GALAXY CLUSTERS AT $z \geqslant 1$: GAS CONSTRAINTS FROM THE SUNYAEV–ZEL'DOVICH ARRAY

T. L. Culverhouse[1,2], M. Bonamente[3,4], E. Bulbul[3], J. E. Carlstrom[1,2,5,6], M. B. Gralla[1,2], C. Greer[1,2], N. Hasler[3],
D. Hawkins[7], R. Hennessy[1,2], N. N. Jetha[3,4], M. Joy[4], J. W. Lamb[7], E. M. Leitch[1,2], D. P. Marrone[1,5,16], A. Miller[8,9,17],
T. Mroczkowski[8,10,11], S. Muchovej[7,11], C. Pryke[1,2,5], M. Sharp[1,6], D. Woody[7], S. Andreon[12], B. Maughan[13],
AND S. A. Stanford[14,15]

[1] Kavli Institute for Cosmological Physics, University of Chicago, Chicago, IL 60637, USA
[2] Department of Astronomy and Astrophysics, University of Chicago, Chicago, IL 60637, USA
[3] Department of Physics, University of Alabama, Huntsville, AL 35899, USA
[4] Space Sciences–VP62, NASA Marshall Space Flight Center, Huntsville, AL 35812, USA
[5] Enrico Fermi Institute, University of Chicago, Chicago, IL 60637, USA
[6] Department of Physics, University of Chicago, Chicago, IL 60637, USA
[7] California Institute of Technology, Owens Valley Radio Observatory, Big Pine, CA 93513, USA
[8] Columbia Astrophysics Laboratory, Columbia University, New York, NY 10027, USA
[9] Department of Physics, Columbia University, New York, NY 10027, USA
[10] Department of Physics and Astronomy, University of Pennsylvania, Philadelphia, PA 19104, USA
[11] Department of Astronomy, Columbia University, New York, NY 10027, USA
[12] INAF-Osservatorio Astronomico di Brera, via Brera 28, 20121, Milano, Italy
[13] HH Wills Physics Laboratory, University of Bristol, Tyndall Ave, Bristol BS8 1TL, UK
[14] University of California, Davis, CA 95618, USA
[15] Institute of Geophysics and Planetary Physics, Lawrence Livermore National Laboratory, Livermore, CA 94550, USA

ABSTRACT

We present gas constraints from Sunyaev–Zel'dovich (SZ) effect measurements in a sample of 11 X-ray and infrared (IR) selected galaxy clusters at $z \geqslant 1$, using data from the Sunyaev–Zel'dovich Array (SZA). The cylindrically integrated Compton-y parameter, Y, is calculated by fitting the data to a two-parameter gas pressure profile. Where possible, we also determine the temperature of the hot intracluster plasma from *Chandra* and *XMM-Newton* data and constrain the gas mass within the same aperture (r_{2500}) as Y. The SZ effect is detected in the clusters for which the X-ray data indicate gas masses above $\sim 10^{13} M_\odot$, including XMMU J2235−2557 at redshift $z = 1.39$, which to date is one of the most distant clusters detected using the SZ effect. None of the IR-selected targets are detected by the SZA measurements, indicating low gas masses for these objects. For these and the four other undetected clusters, we quote upper limits on Y and $M_{\mathrm{gas,SZ}}$, with the latter derived from scaling relations calibrated with lower redshift clusters. We compare the constraints on Y and X-ray-derived gas mass $M_{\mathrm{gas,X\text{-}ray}}$ to self-similar scaling relations between these observables determined from observations of lower redshift clusters, finding consistency given the measurement error.

Key words: cosmic background radiation – cosmology: observations – galaxies: clusters: general – galaxies: clusters: intracluster medium

Online-only material: color figure

1. INTRODUCTION

The Sunyaev–Zel'dovich (SZ) effect is a distortion in the spectrum of the cosmic microwave background (CMB) radiation caused by inverse Compton scattering of CMB photons with the ionized gas in galaxy clusters (Sunyaev & Zel'dovich 1972; Birkinshaw et al. 1991; Carlstrom et al. 2002). The amplitude of the SZ effect is commonly described by the Compton-y parameter, which for a thermal population of electrons is given by the integral of the gas pressure along the line of sight through the cluster:

$$y = \int \frac{\sigma_{\mathrm{T}}}{m_e c^2} P_e \, dl. \qquad (1)$$

In this expression, σ_{T} is the Thomson scattering cross section, m_e is the electron mass, c is the speed of light, P_e is the gas pressure, and the integration is along the line of sight. Integrating y over the solid angle Ω yields the integrated Compton parameter Y, which is proportional to the thermal energy of the cluster (Motl et al. 2005; Bonamente et al. 2008, hereafter B08).

This Letter reports observations of $z \geqslant 1$ clusters made with the Sunyaev–Zel'dovich Array (SZA), and aims to provide constraints on the gas properties of the clusters and a comparison to existing scaling relations. In Section 2, we describe the sample of clusters, Section 3 describes the collection and analysis of the SZA data, and Section 4 presents an analysis of cluster X-ray data (where available) from the *Chandra* and *XMM-Newton* observatories. The results and discussion, including a comparison of SZ and X-ray cluster gas properties, are given in Section 5. Throughout this document, we use the cosmological parameters $H_0 = 73 \ \mathrm{km \, s^{-1} \, Mpc^{-1}}$, $\Omega_m = 0.27$, and $\Omega_\Lambda = 0.73$. Unless otherwise stated, all uncertainties correspond to the 16% and 84% percentiles of the probability distribution function (68% confidence interval).

2. SAMPLE SELECTION

We obtained SZA observations of an ad hoc sample of 11 clusters with $z \geqslant 1$ discovered in either X-ray or infrared (IR)

---

[16] *Hubble* Fellow.
[17] Alfred P. Sloan Fellow.

Table 1
Cluster Sample

| Cluster | z | R.A. | Decl. | Detection, (Ref.)[i] | t_{int}[a] | Short Baselines[b] | | | $D_A^2 Y$[g] | $M_{gas,SZ}$[h] |
| | | | | | | FWHM[c] | σ[d] | B[e] | | |
					(hr)	(arcsec)	(mJy)	(μK)	(10^{-5} Mpc^2)	($10^{13} M_\odot$)
JKCS 041	1.90	02 26 44	−04 41 37	IR, (1)	30.6	86.6 × 96.7	0.13	19.9	<0.68	<0.42
2XMM J083026.2+524133	0.99	08 30 26	+52 41 33	X-ray, (2)	23.3	81.7 × 109.3	0.17	24.4	$2.01^{+0.34}_{-0.32}$	$1.12^{+0.25}_{-0.25}$
RX J0848+4453	1.27	08 48 35	+44 53 49	IR, (3)	44.5	81.4 × 111.6	0.11	15.5	<0.18	<0.28
RX J0849+4452	1.26	08 49 58	+44 51 55	X-ray, (4)	25.5	82.3 × 110.7	0.15	21.1	<0.77	<0.53
RX J0910+5422	1.11	09 10 44	+54 22 09	X-ray, (5)	19.1	83.6 × 107.1	0.17	24.3	<0.29	<0.39
RX J1252−2927	1.24	12 52 54	−29 27 17	X-ray, (6)	12.2	97.8 × 166.9	0.28	22.0	<1.18	<0.72
Cl J1415.1+3612	1.03	14 15 11	+36 12 03	X-ray, (7,8)	55.3[f]	95.9 × 118.1	0.12	13.6	$2.39^{+0.57}_{-0.56}$	$1.26^{+0.36}_{-0.37}$
ISCS1438.1+3338	1.41	14 38 09	+34 14 19	IR, (9)	17.5	110.9 × 129.1	0.21	18.8	<0.36	<0.42
SpARCSJ1638	1.20	16 38 52	+40 38 43	IR, (10)	36.0	78.9 × 108.1	0.13	19.5	<0.70	<0.50
XMMU J2235−2557	1.39	22 35 21	−25 57 42	X-ray, (11)	42.1	103.7 × 150.8	0.14	11.5	$1.87^{+0.34}_{-0.33}$	$0.96^{+0.24}_{-0.24}$
XMMXCS J2215.9−1738	1.46	22 15 58	−17 38 03	X-ray, (12)	10.8	107.8 × 130.1	0.25	22.8	<0.32	<0.38

Notes.

[a] On-source integration time, unflagged data.

[b] Short baselines correspond to (0–2 kλ).

[c] Synthesized beam approx. FWHM.

[d] Achieved rms noise in short-baseline maps.

[e] Corresponding brightness sensitivity in short-baseline maps.

[f] 34.1 hr of "V-array" integration from Muchovej et al. (2007); 21.2 hr from "L-array."

[g] Y constraints from SZA data. Where there are sufficient X-ray counts to determine r_{2500} (see Table 3), Y is calculated within this radius; otherwise, an angular aperture of radius 30 arcsec is used. Upper limits are calculated at 95% confidence.

[h] $M_{gas,SZ}$ determined from Y constraints and scaling relations from Bonamente et al. (2008) and are independent of the X-ray-determined gas mass $M_{gas,X-ray}$.

[i] Cluster references: (1) Andreon et al. 2009; (2) Lamer et al. 2008; (3) Stanford et al. 1997; (4) Rosati et al. 1999; (5) Stanford et al. 2002; (6) Rosati et al. 2004; (7) Redshift from Maughan et al. 2006; (8) Perlman et al. 2002; (9) Stanford et al. 2005; (10) Muzzin et al. 2009; (11) Mullis et al. 2005; (12) Stanford et al. 2006.

imaging surveys—basic information about the clusters are given in Table 1. Surveys in these bands can yield large numbers of high-redshift cluster candidates using a variety of methods. These include the red sequence in the optical (Gladders & Yee 2000, 2005), its extension into the IR (Stanford et al. 2005; Andreon et al. 2009; Eisenhardt et al. 2008; Muzzin et al. 2009), and imaging surveys and/or serendipitous detection in X-rays (e.g., Stanford et al. 2006; Lamer et al. 2008). X-ray observations provide direct evidence for the hot plasma which typically constitutes ∼10% of the cluster total mass; seven clusters in the sample are the most massive X-ray-detected systems at redshift above one. Since this is the same plasma which causes the SZ effect, clusters in the sample originally detected in X-rays are expected to have significant SZ signal, provided they are of sufficient gas mass and temperature.

The IR-detected clusters in the sample were selected as optically rich candidates with properties typical of massive clusters: ISCS1438.1+3338 was detected in the *Spitzer*/IRAC Shallow Survey as an overdensity of galaxies with photometric redshifts between $1.3 < z < 1.5$; member galaxies were confirmed with Keck optical spectroscopy to have $\Delta z = 0.01$. One of the richest, spectroscopically confirmed clusters from the SpARCS North Survey is SpARCSJ1638, with initial detection via two-filter imaging. JKCS 041 was discovered using a modified red-sequence method applied to *J*- and *K*-band data in the UKIRT Infrared Deep Sky Survey, with a derived photometric redshift of 1.9; *Chandra* follow-up revealed a low luminosity, diffuse source of X-ray emission at the cluster location. Also discovered in the IR, member galaxies of RX J0848+4453 exhibit very red *J–K* colors, with follow-up spectroscopy confirming that the member redshifts are within $\Delta z = 0.002$ of each other. This cluster has also been observed in the X-ray with *Chandra*; Santos et al. (2008) present a recent analysis.

The most massive, high-redshift cluster candidates in these different surveys provide a starting point for studies of the SZ effect in galaxy clusters at $z \geqslant 1$. Constraints on Y from the SZ effect alone provide useful information on the presence of hot gas, while joint analysis with X-ray data allows comparison with more local samples via scaling relations, to test for evolutionary effects.

3. SUNYAEV–ZEL'DOVICH EFFECT ANALYSIS

3.1. SZA Observations

The SZA is an interferometric array comprising eight 3.5 m telescopes, capable of observations in an 8 GHz wide band centered on 31 GHz or 90 GHz. The instrument was configured to operate at 31 GHz for the observations reported here—see Muchovej et al. (2007) for further details. The field of view of the SZA is given by the primary beam of a single telescope, of FWHM approximately $11'$ at the center of the 31 GHz band, with typical system temperatures ∼40 K at this frequency.

Observations of each cluster were performed with different array configurations. All observations of ISCS1438.1+3338 and two-thirds of the tracks on Cl J1415.1+3612 were observed from the OVRO valley floor site, using a compact six-telescope plus two outrigger array, denoted "V" array here. JKCS 041 was initially observed for 12 days at the CARMA site. An imaging array configuration (denoted "I") was used, with no outriggers but higher sensitivity to typical cluster angular scales. A further 8 days of data were taken in a "low dec" plus outrigger array, or "L" array. This configuration is similar to "V" array, but with the array stretched north–south to prevent excessive shadowing for low declination clusters. Tracks on all other clusters were taken in "L" array.
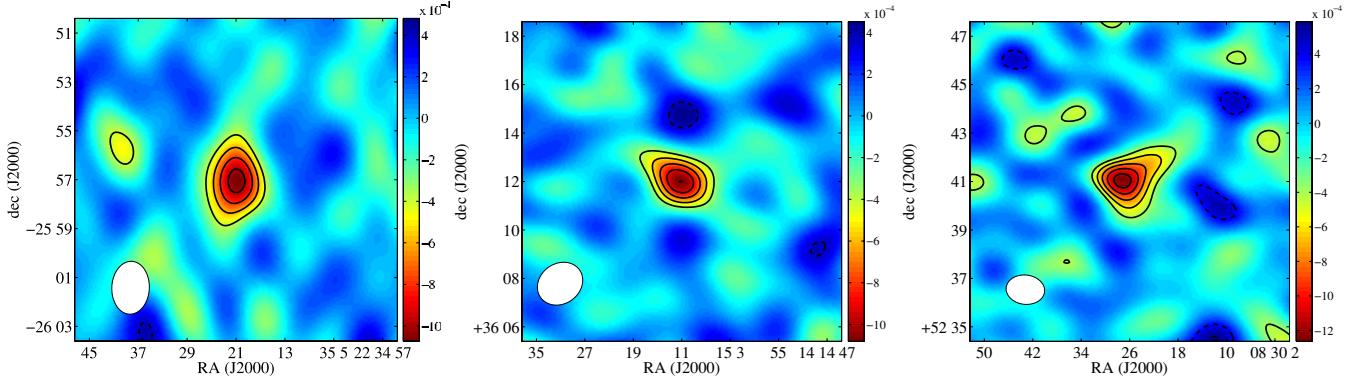
Figure 1. CLEANed SZA short ($<2\,k\lambda$) baseline images of the three clusters with significant SZ effect detections: left to right, XMMU J2235−2557, Cl J1415.1+3612, and 2XMM J083026.2+524133, with the color scale in Jy beam^{-1}. The contours begin at 2σ and are spaced at unit intervals of the map rms σ. The white ellipse represents the half-power point of the elliptical Gaussian that approximates the main lobe of the synthesized beam. Radio sources have been removed for display purposes.

(A color version of this figure is available in the online journal.)

Pairs of close-packed telescopes form short baselines (typically of order 4–20 m or 0.4–2 kλ), which are sensitive to the signal from clusters on angular scales of order $1'$. The outrigger telescopes form long baselines (50 m or 2–10 kλ) between themselves and the close-packed antennas; these baselines allow measurement of contaminating radio sources which could otherwise mask the SZ effect. The long-baseline dirty map noise is typically $\sim$0.2 mJy, with resolution $\sim$20$''$. Further details of the SZA observations presented here, including on-source integration time and sensitivity and effective resolution (the synthesized beam) of the short-baseline maps, are given in Table 1.

SZA data are processed in a pipeline developed within the SZA collaboration for the reduction and calibration of interferometric data, described in detail in Muchovej et al. (2007). The pipeline produces calibrated visibilities—samples of the Fourier transform of the sky brightness distribution multiplied by the primary beam:

$$V(u, v) = \int_{-\infty}^{+\infty} \int_{-\infty}^{+\infty} A_N(l, m) I(l, m) e^{-2\pi i[ul+vm]} dl\, dm, \quad (2)$$

where $A_N(l, m)$ is the normalized antenna beam pattern, $I(l, m)$ is the sky intensity distribution, u and v are the baseline lengths projected onto the sky, and l and m are direction cosines measured with respect to the (u, v) axes. Fourier transforming the visibility data gives the sky convolved with the synthesized beam or the "dirty map."

Figure 1 presents CLEANed images made from only the SZA short-baseline data of the clusters in the sample for which we detect the SZ effect at $>5\sigma$, i.e., 2XMM J083026.2+524133, Cl J1415.1+3612, and XMMU J2235−2557. Comparing the image data and the synthesized beam, we note that the SZ effect is only partially resolved for each detected cluster. Radio sources have been identified and removed using the long and short-baseline data. Unresolved radio sources were found within $1'$ of the cluster center in Cl J1415.1+3612 and XMMU J2235−2557. Resolved emission from two low-redshift galaxies was detected: from NGC 5529 $4\rlap{.}'9$ from the Cl J1415.1+3612 position and from NGC 7314 $7\rlap{.}'8$ from the XMMU J2235−2557 position. No cluster in the sample has more than three detected radio sources within the SZA field of view.

3.2. Constraints on the Integrated SZ Effect Signal

For each cluster, Y is constrained by fitting a model to the data; the model y map is generated by integrating a gas pressure profile along the line of sight as in Equation (1). The y map is multiplied by the primary beam, Fourier transformed, interpolated at the (u, v) coordinates of the measured visibilities and the χ^2 evaluated for the model against the data. We use the spherically symmetric Nagai et al. (2007) model which describes the pressure as a function of radius r as

$$P_e(r) = \frac{P_{e,i}}{(r/r_p)^c[1 + (r/r_p)^a]^{(b-c)/a}}. \quad (3)$$

In Equation (3), $P_{e,i}$ is the pressure normalization, r_p is the characteristic scale radius, and a, b, and c are parameters describing profile slopes at intermediate ($r \approx r_p$), outer ($r > r_p$), and inner ($r \ll r_p$) radii. As in Mroczkowski et al. (2009), the power-law indices of the pressure model are held fixed at $(a, b, c) = (0.9, 5.0, 0.4)$.

The Monte Carlo Markov chain (MCMC) method described in Bonamente et al. (2004) is used to determine the probability distributions of the free cluster model parameters r_p and $P_{e,i}$; positions of clusters without a significant decrement are fixed to the values in Table 1, but are otherwise variable. Following Muchovej et al. (2007), an elliptical Gaussian is used to model the two resolved galaxies found in the sample (Section 3.1), while unresolved sources are described by one amplitude and two position parameters—the typical rms on unresolved source position is of order 0.3 arcsec. The free parameters of the cluster, resolved, and unresolved source models are determined simultaneously with the MCMC method. Accepted $(r_p, P_{e,i})$ parameter pairs in the MCMC analysis are used to calculate the cylindrically integrated Y parameter over the solid angle of the cluster, via Equations (1) and (3).

For clusters with $\geqslant 300$ X-ray source photons, we measure Y out to a radius of r_{2500} as determined from the X-ray data (see Table 3), where r_Δ is defined as the radius at which the mean cluster density falls to Δ times the critical density at the cluster redshift $\rho_c(z)$:

$$\frac{4}{3}\pi\, \rho_c(z)\, \Delta\, r_\Delta^3 = M_{\text{tot}}(r_\Delta). \quad (4)$$

The choice of $\Delta = 2500$ allows our Y parameters to be compared directly to the scaling relations of B08, which were

Table 2
Chandra and *XMM-Newton* Observations

Cluster	ObsID	Detector	Exposure Time (ks)	Source Photons	n(H) Column Density (10^{20} cm^{-2})
2XMM J083026.2+524133	0092800201	MOS1, PN	60.0, 55.9	2495[b]	4.2
Cl J1415.1+3612	4163	ACIS-I	86.9	1395[a]	1.1
RX J0910+5422	2227, 2452	ACIS-I	161.2	411[a]	1.9
RX J1252−2927	4198	ACIS-I	161.4	540[a]	6.1
RX J0849+4452	1708, 927	ACIS-I	186.6	392[a]	2.8
RX J0848+4453	1708, 927	ACIS-I	186.6	144[a]	2.8
XMMU J2235−2557	6975, 6976, 7367, 7368, 7404	ACIS-S	195.5	1532[b]	1.5
XMMXCS J2215.9−1738	7919, 8566	ACIS-S	85.9	161[b]	2.0
	0106660601	MOS1, MOS2, PN	81.0, 82.1, 60.0		
	0106660101	MOS1, MOS2, PN	55.8, 53.1, 42.7		
	0106660201	MOS1,MOS2,PN	35.7, 37.7, 24.5	686[b]	2.0
JKCS 041	9368	ACIS-S	78.8	114[b]	2.3

Notes.
[a] 0.7–7 keV band.
[b] 0.5–7 keV band.
[c] Source photons are for a cluster-centric region of radius <30 arcsec, except 2XMM J083026.2+524133 and Cl J1415.1+3612 for which we use <60 arcsec. In comparison with Andreon et al. (2009), who find 223 source photons for JKCS 041 in a 60 arcsec aperture between 0.2 and 2 keV, we find 230 source photons in our 0.5–7 keV band in a 60 arcsec aperture.

derived with $Y(<r_{2500})$ for a large sample of low-to-intermediate redshift clusters. A fixed angular aperture of radius 30″ is used for clusters with <300 X-ray photons, evaluating $Y(<30″)$ rather than $Y(<r_{2500})$ (such clusters are not compared to the scaling relations).

The mean ($D_A^2 \bar{Y}$) and 68% confidence intervals are calculated from the resultant probability distributions of $D_A^2 Y$. If $D_A^2 \bar{Y} > 3\sigma_l$, where σ_l is the 14th percentile of the distribution, we quote the mean and 68% confidence interval for each cluster. If $D_A^2 \bar{Y} < 3\sigma_l$, we quote the 95% confidence upper limit on $D_A^2 Y$. The results are presented in Table 1, along with the equivalent gas mass constraints calculated from the low-redshift $Y-M_{gas,X-ray}$ scaling relation of B08, which assumes self-similar evolution as $\log_{10}(Y D_A^2 E(z)^{-2/3}) = A + B\log_{10}(M_{gas})$, with $A = -23.25$ and $B = 1.41$ taken from all clusters in their sample. Errors on $M_{gas,SZ}$ include the uncertainty in the low-redshift scaling relation parameters as well as the uncertainty in Y, but do not include errors introduced by geometric effects when performing the cylindrical integral or the intrinsic scatter in Y at fixed M_{gas}.[18]

Note that these mass constraints are entirely independent of the $M_{gas,X-ray}$ calculated in the following X-ray analysis and serve as the only gas mass estimates available for clusters with insufficient X-ray data.

4. X-RAY OBSERVATIONS AND DATA ANALYSIS

4.1. Chandra and XMM-Newton Data Analysis

We analyzed *Chandra* and *XMM-Newton* observations for each cluster that has archival data.

The *Chandra* event files were reprocessed in CIAO 4.1 in order to apply the latest calibration available (CALDB 4.1). Periods of high background were excised following the prescription of Markevitch et al. (2003). A peripheral region

---

[18] The apparent difference between the SZ-derived gas mass for Cl J1415.1+3612 presented here and that in Muchovej et al. (2007) is due to the different r_{2500} used; their value is reproduced from an earlier analysis of *XMM-Newton* data by Maughan et al. (2006), compared to our *Chandra* derivation in Section 4. When the same r_{2500} is used, the gas masses are consistent, as expected.

60″–120″ from the cluster center was used to determine the local background; this region allows the background to be determined from the same chip as the cluster, given the limited angular size of the sources. This choice minimizes the effect of the temporal and spatial variability of the Galactic soft X-ray emission (e.g., Snowden et al. 1997).

For the spectral analysis of each cluster, we extracted individual spectra and matching response files from each observation separately (Table 2).

The cluster 2XMM J083026.2+524133 was detected serendipitously in two pointed *XMM-Newton* observations (Lamer et al. 2008), and these observations are the only available X-ray data for this cluster. We analyze the longest of the two observations, in which the cluster was detected in two of the three detectors, MOS1 and PN (Table 2). For cluster XMMXCS J2215.9−1738, we analyze both the *Chandra* data and the three longest observations with *XMM-Newton*.

The *XMM-Newton* data were reduced using the SAS 9.0 software and the calibration data available as of 2009 July, and according to the method described in Nevalainen et al. (2005). In particular, periods of high background that affected the second half of the observation were excluded. We used a local background as measured in a peripheral region of each detector, similar to the method used for the *Chandra* data.

For the purpose of mass calculation and comparison to known scaling relations, we elected to only use clusters for which archival data are available, and with at least 300 source photons. This selection leaves us with seven clusters: 2XMM J083026.2+524133, Cl J1415.1+3612, RX J0910+5422, RX J0849+4452, RX J1252−2927, XMMU J2235−2557, and XMMXCS J2215.9−1738.

4.2. Image Analysis

Event files for each cluster were merged if more than one observation was available, and images extracted using photons in the 0.7–7 keV band for ACIS-I observations, and in the 0.5–7 keV band for ACIS-S, EPIC-MOS, and EPIC-PN observations (see Table 2). The same table also presents the number of source photons, after subtracting the expected number of background photons from the peripheral region.

Table 3
Image and Spectral Analysis of the X-ray Data

Cluster	kT (keV)	L_X (10^{44} erg s^{-1})	n_{e0} (10^{-2} cm^{-3})	r_c (arcsec)	β	r_{2500} (arcsec)	$M_{\text{gas,X-ray}}$ ($10^{13} M_\odot$)
2XMM J083026.2+524133[b]	$7.6^{+0.8}_{-0.8}$	16^{+1}_{-1}	$0.83^{+0.03}_{-0.03}$	$28.6^{+1.0}_{-0.9}$	0.7	$38.8^{+2.0}_{-2.7}$	$1.40^{+0.14}_{-0.20}$
Cl J1415.1+3612[a]	$6.5^{+0.9}_{-0.8}$	10^{+1}_{-1}	$2.25^{+0.14}_{-0.14}$	$10.9^{+0.4}_{-0.4}$	0.7	$39.4^{+2.9}_{-2.9}$	$1.10^{+0.08}_{-0.08}$
RX J1252$-$2927[a]	$6.6\pm^{1.5}_{1.2}$	$3.6^{+0.4}_{-0.4}$	$1.14^{+0.12}_{-0.09}$	$13.2^{+0.9}_{-0.9}$	0.7	$32.1^{+3.6}_{-4.1}$	$0.66^{+0.09}_{-0.10}$
RX J0910+5422[a]	$4.5^{+1.5}_{-0.9}$	$1.7^{+0.2}_{-0.2}$	$0.65^{+0.09}_{-0.08}$	$17.9^{+3.0}_{-1.7}$	0.7	$26.6^{+4.2}_{-5.2}$	$0.35^{+0.08}_{-0.10}$
RX J0849+4452[a]	$6.7^{+2.0}_{-1.5}$	$2.1^{+0.4}_{-0.4}$	$0.67^{+0.08}_{-0.07}$	$12.1^{+1.1}_{-1.0}$	0.7	$32.4^{+4.7}_{-5.0}$	$0.32^{+0.07}_{-0.07}$
XMMU J2235$-$2557[b]	$9.0^{+1.5}_{-1.2}$	$6.9^{+0.4}_{-0.4}$	$1.47^{+0.08}_{-0.08}$	$12.6^{+0.6}_{-0.5}$	0.7	$36.9^{+3.4}_{-3.6}$	$0.95^{+0.11}_{-0.12}$
XMMXCS J2215.9$-$1738[b]	$7.4\pm^{2.1}_{1.4}$	$2.2 \pm +0.1$	$0.58\pm^{0.05}_{0.04}$	$19.6\pm^{1.2}_{1.4}$	0.7	$27.5\pm^{3.3}_{3.5}$	0.38 ± 0.09

Notes.
[a] 0.7–7 keV used for spectral analysis.
[b] 0.5–7 keV used for spectral analysis.

The gas density is described using an isothermal β model which, given the limited number of source photons, provides a good fit to all clusters with X-ray data:

$$n_e(r) = \frac{n_{e,0}}{[1 + (r/r_c)^2]^{3\beta/2}}. \qquad (5)$$

Model parameters $n_{e,0}$ and r_c are constrained using a Markov chain Monte Carlo method described in Bonamente et al. (2004) and are presented in Table 3. We fix $\beta = 0.7$ throughout. Use of the beta model permits a direct comparison with the scaling relations presented in B08, obtained using the same isothermal model.

4.3. Spectral Analysis

The spectra for each cluster were extracted from a circular region about the centroid of the X-ray emission given in Table 1. A radius of $<30''$ was used for all clusters except 2XMM J083026.2+524133 and Cl J1415.1+3612, for which we use $<60''$; the background spectrum was extracted from the surrounding $60''$–$120''$ region. Given the limited signal-to-noise ratio of the spectra, the metal abundances were fixed at a fiducial value of $A = 0.3 Z_\odot$ for all clusters. This approximation has a negligible impact on the results of our analysis.

We performed spectral fits to an optically thin model using the APEC emissivity code (Smith et al. 2001); the redshift, Galactic H I column density (Table 2), and solar abundance are fixed for each cluster leaving just the electron temperature and a normalization constant. The resulting electron temperatures are presented in Table 3.

4.4. Mass Measurement

The gas model parameters determined from the X-ray images and spectral constraints on the gas temperature are used to measure the X-ray gas mass $M_{\text{gas,X-ray}}$. This is calculated via a spherical integration of n_e out to r_{2500} for each sample in the Markov chain; this choice of radius allows a comparison of Y and $M_{\text{gas,X-ray}}$ to the scaling relations of B08. The values of r_{2500} and $M_{\text{gas,X-ray}}$ of each cluster are shown in Table 3, with the comparison to Y and previously measured scaling relations in Figure 2. Systematic errors in the measurement of the gas temperature are a source of uncertainty in the estimate of gas masses (e.g., Reese et al. 2010; Nevalainen et al. 2010). We estimate that a 10% systematic error in the temperature causes a change in r_{2500} by 2%, and this change in the radius of integration results in a variation by 4% in the gas mass at r_{2500}.
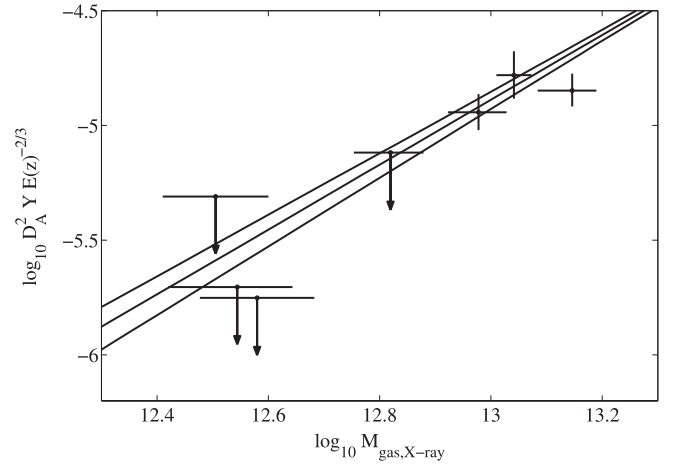
Figure 2. Comparison of the Y upper limits and detections to $M_{\text{gas,X-ray}}$ within r_{2500}, assuming self-similar evolution. The solid lines are the scaling relation measured at r_{2500} by B08, and its 1σ uncertainties. In order of X-ray gas mass, the clusters are RX J0849+4452, RX J0910+5422, XMMXCS J2215.9$-$1738, RX J1252$-$2927, XMMU J2235$-$2557, Cl J1415.1+3612, and 2XMM J083026.2+524133.

5. RESULTS AND DISCUSSION

The SZA observations presented here demonstrate the efficacy of using the SZ effect as a cluster mass discriminator, independent of redshift. The SZ effect of the high mass clusters in the ad hoc sample of $z > 1$ clusters was detected with SZA integration times comparable to those required for similar mass clusters at low redshifts. Specifically, the SZ effect was detected in the three clusters for which $M_{\text{gas,X-ray}} \gtrsim 10^{13} M_\odot$ and temperature $\geqslant 6.5$ keV as determined independently from X-ray data (see Table 3). The most distant cluster detected by the SZA is XMMU J2235$-$2557 at $z = 1.39$, which has a total mass within r_{500} of $M_{500} = (4.4 \pm 1.0) \times 10^{14} M_\odot$ (Rosati et al. 2009). Weak lensing observations by Jee et al. (2009) indicate a total mass within 1 Mpc of $(8.3 \pm 1.7) \times 10^{14} M_\odot$. For 2XMM J083026.2+524133 and Cl J1415.1+3612, M_{500} are $(5.6 \pm 1.0) \times 10^{14} M_\odot$ (Lamer et al. 2008) and $3.0^{+1.0}_{-0.7} \times 10^{14} M_\odot$, respectively, with the latter derived from the data in Maughan et al. (2006).

The lack of SZ detections for the other clusters strongly indicates that they are lower mass systems; in particular, those originally discovered in the infrared have $M_{\text{gas}} < 5 \times 10^{12} M_\odot$ (see Table 1) and their null detection prevents investigation of optical–SZ scalings.

As a first step in investigating the SZ–mass scaling relationship at high redshift, we plot in Figure 2 the integrated Compton Y values against the X-ray gas mass determinations, assuming self-similar evolution. The clusters plotted include only those with robust X-ray gas mass constraints (see Table 3). For comparison with low-redshift clusters, the solid lines in Figure 2 show the Y–$M_{\mathrm{gas,X\text{-}ray}}$ scaling relationship presented in B08 and its 1σ uncertainties. The figure illustrates that there is good agreement between the scaling of the high-z clusters and that found in the low-redshift sample. Measurements of more clusters are needed, however, to make a more definitive comparison. Ongoing SZ surveys from instruments such as the Atacama Cosmology Telescope (Fowler et al. 2007) and the South Pole Telescope (Carlstrom et al. 2009) will provide much larger samples of SZ-selected clusters at high redshift (e.g., Vanderlinde et al. 2010).

REFERENCES

Andreon, S., Maughan, B., Trinchieri, G., & Kurk, J. 2009, A&A, 507, 147
Birkinshaw, M., Hughes, J. P., & Arnaud, K. A. 1991, ApJ, 379, 466
Bonamente, M., Joy, M., LaRoque, S. J., Carlstrom, J. E., Nagai, D., & Marrone, D. P. 2008, ApJ, 675, 106
Bonamente, M., Joy, M. K., Carlstrom, J. E., Reese, E. D., & LaRoque, S. J. 2004, ApJ, 614, 56
Carlstrom, J. E., Holder, G. P., & Reese, E. D. 2002, ARA&A, 40, 643
Carlstrom, J., et al. 2009, arXiv:0907.4445
Eisenhardt, P. R. M., et al. 2008, ApJ, 684, 905
Fowler, J., et al. 2007, Appl. Opt., 46, 3444
Gladders, M. D., & Yee, H. K. C. 2000, AJ, 120, 2148
Gladders, M. D., & Yee, H. K. C. 2005, ApJS, 157, 1
Jee, M. J., et al. 2009, ApJ, 704, 672
Lamer, G., Hoeft, M., Kohnert, J., Schwope, A., & Storm, J. 2008, A&A, 487, L33
Markevitch, M., et al. 2003, ApJ, 583, 70
Maughan, B. J., Jones, L. R., Ebeling, H., & Scharf, C. 2006, MNRAS, 365, 509
Motl, P. M., Hallman, E. J., Burns, J. O., & Norman, M. L. 2005, ApJ, 623, L63
Mroczkowski, T., et al. 2009, ApJ, 694, 1034
Muchovej, S., et al. 2007, ApJ, 663, 708
Mullis, C. R., Rosati, P., Lamer, G., Böhringer, H., Schwope, A., Schuecker, P., & Fassbender, R. 2005, ApJ, 623, L85
Muzzin, A., et al. 2009, ApJ, 698, 1934
Nagai, D., Vikhlinin, A., & Kravtsov, A. V. 2007, ApJ, 655, 98
Nevalainen, J., David, L., & Guainazzi, M. 2010, arXiv:1008.2102
Nevalainen, J., Markevitch, M., & Lumb, D. 2005, ApJ, 629, 172
Perlman, E. S., Horner, D. J., Jones, L. R., Scharf, C. A., Ebeling, H., Wegner, G., & Malkan, M. 2002, ApJS, 140, 265
Reese, E. D., Kawahara, H., Kitayama, T., Ota, N., Sasaki, S., & Suto, Y. 2010, ApJ, 721, 653
Rosati, P., Stanford, S. A., Eisenhardt, P. R., Elston, R., Spinrad, H., Stern, D., & Dey, A. 1999, AJ, 118, 76
Rosati, P., et al. 2004, AJ, 127, 230
Rosati, P., et al. 2009, A&A, 508, 583
Santos, J. S., Rosati, P., Tozzi, P., Böhringer, H., Ettori, S., & Bignamini, A. 2008, A&A, 483, 35
Smith, R. K., Brickhouse, N. S., Liedahl, D. A., & Raymond, J. C. 2001, ApJ, 556, L91
Snowden, S. L., et al. 1997, ApJ, 485, 125
Stanford, S. A., Elston, R., Eisenhardt, P. R., Spinrad, H., Stern, D., & Dey, A. 1997, AJ, 114, 2232
Stanford, S. A., Holden, B., Rosati, P., Eisenhardt, P. R., Stern, D., Squires, G., & Spinrad, H. 2002, AJ, 123, 619
Stanford, S. A., et al. 2005, ApJ, 634, L129
Stanford, S. A., et al. 2006, ApJ, 646, L13
Sunyaev, R. A., & Zel'dovich, Y. B. 1972, Comments Astrophys. Space Phys., 4, 173
Vanderlinde, K., et al. 2010, ApJ, 722, 1180